

RESEARCH ARTICLE SUMMARY

MICROBIOTA

Microbe-mediated intestinal NOD2 stimulation improves linear growth of undernourished infant mice

Martin Schwarzer*, Umesh Kumar Gautam, Kassem Makki, Anne Lambert, Tomáš Brabec, Amélie Joly, Dagmar Šrůtková, Pierre Poinso, Tereza Novotná, Stéphanie Geoffroy, Pascal Courtin, Petra Petr Hermanová, Renata C. Matos, Jonathan J. M. Landry, Céline Gérard, Anne-Laure Bulteau, Tomáš Hudcovic, Hana Kozáková, Dominik Filipp, Marie-Pierre Chapot-Chartier, Marek Šinkora, Noël Peretti, Ivo Gomperts Boneca, Mathias Chamaillard, Hubert Vidal, Filipe De Vadder, François Leulier*

INTRODUCTION: Growth in size and weight is an intrinsic process in each individual's ontogeny. The highest rate of growth takes place after birth and in mammals is governed by the somatotrophic axis, where growth hormone (GH) instructs the liver and peripheral tissues to produce insulin-like growth factor-1 (IGF-1) to promote organ and systemic growth. Nutrition is paramount to growth, and chronic undernutrition triggers a state of GH resistance manifested by low circulating IGF-1, leading to stunting. Recent studies have shown that not only nutrients but also components of the intestinal microbiota can be critical in shaping host growth dynamics. Previously, we established that the intestinal microbiota is necessary to buffer the deleterious effect of chronic undernutrition on mouse systemic postnatal growth. We showed that microbial stimulation supports the activity of the somatotrophic axis in juveniles by improving the GH sensitivity of peripheral tissues and increasing the circulating levels of IGF-1. Furthermore, using monoxenic mice, we showed that a strain of

Lactiplantibacillus plantarum (strain Lp^{WJL}), which was selected because of its ability to promote growth in a *Drosophila* model of diet-induced stunting, recapitulates the beneficial effects of a complex microbiota on the somatotrophic axis and juvenile growth of malnourished mice in a strictly strain-dependent manner.

RATIONALE: Here, we studied the effect Lp^{WJL} on mouse postnatal growth in a new preclinical model of diet-induced stunting in conventional animals. We investigated both the bacterial cues and host mechanisms underpinning the complex local and whole-body adaptations triggered by such intestinal bacterium leading to improved systemic growth despite chronic undernutrition.

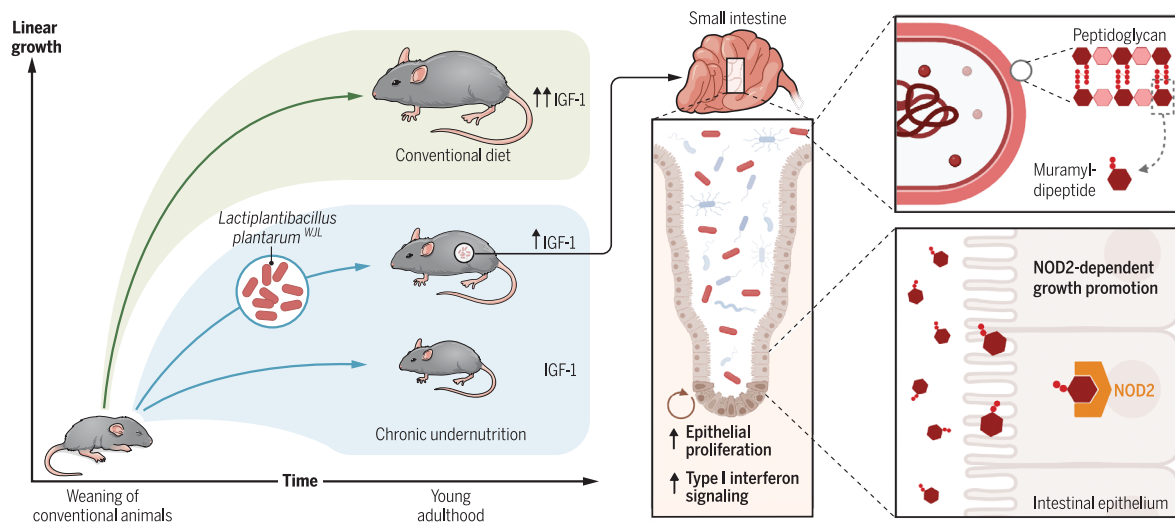
RESULTS: We report a new preclinical mouse model of diet-induced stunting in conventional mice without small intestinal inflammation but associated with altered crypt cell proliferation. Using this model, we show that Lp^{WJL} sustains the postnatal growth of malnourished conven-

tional animals by orchestrating metabolic and hormonal changes in the juvenile host manifested as improved circulating levels and activity of IGF-1 and insulin. We identified cell walls isolated from Lp^{WJL}, as well as ligands of the pattern recognition receptor NOD2, as being sufficient bacterial cues stimulating animal growth. Further, we found that NOD2 is necessary in intestinal epithelial cells for Lp^{WJL}-mediated improvement of intestinal crypt cell proliferation, type I interferon-regulated gene induction, IGF-1 production, and postnatal growth promotion in malnourished conventional animals.

CONCLUSION: Our results demonstrate that bacterial cell walls or purified NOD2 ligands are sensed by the pattern recognition receptor NOD2 in the intestinal epithelial cells and sustain postnatal juvenile growth despite chronic undernutrition. We posit that one of the mechanisms by which Lp^{WJL} and its cell wall exert its postnatal growth-promoting properties is the buffering of the deleterious effect of undernutrition on small intestinal crypt cell proliferation through NOD2-dependent bacterial cell walls sensing. Our results suggest that, coupled with renutrition strategies, supplementation of evidence-based probiotics such as Lp^{WJL} or defined bacteria-derived postbiotics such as Lp^{WJL} cell walls and/or NOD2 agonists have the potential to alleviate persistent stunting, one of the long-term sequelae of undernutrition that still affects >149 million children under 5 years of age in low- and middle-income countries. ■

The list of author affiliations is available in the full article.
*Corresponding author. Email: schwarzer@biomed.cas.cz (M.S.); francois.leulier@ens-lyon.fr (F.L.)

READ THE FULL ARTICLE AT
<https://doi.org/10.1126/science.ade9767>



Lp^{WJL} or its purified cell wall improves the growth of undernourished infant mice through intestinal NOD2 signaling. Chronic undernutrition after weaning leads to stunting, which is alleviated by Lp^{WJL}. Lp^{WJL} peptidoglycans engage NOD2 in the intestinal epithelium, which increases the proliferation of small intestinal stem cells, type I interferon signaling, IGF-1 production, and postnatal growth despite undernutrition.

MICROBIOTA

Microbe-mediated intestinal NOD2 stimulation improves linear growth of undernourished infant mice

Martin Schwarzer^{1,2*}, Umesh Kumar Gautam¹, Kassem Makki^{2,3,†}, Anne Lambert², Tomáš Brabec⁴, Amélie Joly², Dagmar Šrůtková¹, Pierre Poinso^{2,3,5}, Tereza Novotná¹, Stéphanie Geoffroy^{2,†}, Pascal Courtin⁶, Petra Petr Hermanová¹, Renata C. Matos², Jonathan J. M. Landry⁷, Céline Gérard³, Anne-Laure Bulteau^{2,§}, Tomáš Hudcovic¹, Hana Kozáková¹, Dominik Filipp⁴, Marie-Pierre Chapot-Chartier⁶, Marek Šinkora¹, Noël Peretti^{3,5}, Ivo Gomperts Boneca⁸, Mathias Chamillard⁹, Hubert Vidai³, Filipe De Vadder², François Leulier^{2,*}

The intestinal microbiota is known to influence postnatal growth. We previously found that a strain of *Lactiplantibacillus plantarum* (strain Lp^{WJL}) buffers the adverse effects of chronic undernutrition on the growth of juvenile germ-free mice. Here, we report that Lp^{WJL} sustains the postnatal growth of malnourished conventional animals and supports both insulin-like growth factor-1 (IGF-1) and insulin production and activity. We have identified cell walls isolated from Lp^{WJL}, as well as muramyl dipeptide and mifamurtide, as sufficient cues to stimulate animal growth despite undernutrition. Further, we found that NOD2 is necessary in intestinal epithelial cells for Lp^{WJL}-mediated IGF-1 production and for postnatal growth promotion in malnourished conventional animals. These findings indicate that, coupled with renutrition, bacteria cell walls or purified NOD2 ligands have the potential to alleviate stunting.

Linear and ponderal growth is an inherent capacity of all juvenile multicellular organisms. In mammals, postnatal growth is controlled by the somatotrophic axis, where growth hormone (GH) instructs the liver and peripheral tissues to produce insulin-like growth factor-1 (IGF-1) to promote organ and systemic growth (1). Next to IGF-1, insulin is the main anabolic hormone of the body, regulating carbohydrate, lipid, and protein metabolism (2). Although the somatotrophic axis is of key importance during growth, a coordinated regulation of metabolism is required to provide substrates and fuels to the growing tissues. As a consequence, insulin also influences animal development and growth (3).

Nutrition is paramount to growth, and chronic undernutrition triggers a state of GH resistance manifested by low circulating IGF-1, leading to stunting (4, 5). In addition to its influence on nutrition, the microbial environment also shapes systemic growth (6, 7). Acute malnutrition triggers an altered maturation of the intestinal microbiota in malnourished children, which contributes to stunting and wasting (8, 9), and the absence of microbial stimulation has negative impacts on the circulating levels of IGF-1 (10, 11) and insulin (12) in germ-free mice.

Previously, we established that the intestinal microbiota is necessary to maximize mouse systemic postnatal growth under normal nutritional conditions and during chronic undernutrition (10). We showed that microbial stimulation supports the activity of the somatotrophic axis in juveniles by improving the GH sensitivity of peripheral tissues and increasing the circulating levels of IGF-1 (10). Furthermore, using monoxenic mice, we showed that a strain of *Lactiplantibacillus plantarum* (strain Lp^{WJL}), which was selected because of its ability to promote growth in a *Drosophila* model of diet-induced stunting (13), recapitulates the beneficial effects of the complex microbiota on the somatotrophic axis and on the juvenile growth of well-fed or malnourished mice in a strictly strain-dependent manner (10).

Here, we build on these results and study the effect of Lp^{WJL} on the postnatal growth in a new preclinical model of diet-induced stunting in conventional animals and investigate the mechanisms by which this specific intestinal bacterium triggers a complex, whole-body adaptation leading to enhanced systemic growth.

Results

Diet-induced stunting in conventional mice

On the basis of our previous findings (10), we aimed to model chronic undernutrition in conventional mice. To this end, we designed an AIN93G-based modified isocaloric diet low in fat and protein [malnourished (MAL)] (table S1 and Fig. 1B). The macroscopic growth parameters (weight and size gains) of C57Bl/6J male mice weaned on MAL diet were severely altered compared with mice weaned on an AIN93G diet [conventional (CON)] (table S1 and Fig. 1, A to K). At postnatal day 56, MAL mice were stunted and had shorter body size (Fig. 1, A and C to E) and femur bone length (Fig. 1, F and G) compared with CON mice. The diminished length gain was accompanied by lower global weight gain, as well as a lower final weight of individual organs (Fig. 1, H to K). The stunted phenotype of MAL-fed animals was not the result of an alteration of the food intake compared with the CON-fed group; the relative food intake was even increased on the MAL diet during the last week of the protocol (fig. S1). Feeding the MAL diet to male mice of another genetic background (BALB/c) resulted in a similar phenotype (fig. S2).

Recently, Brown *et al.* (14) reported a mouse model of environmental enteropathy (EE) resulting in a moderately stunted phenotype. EE is a poorly understood disorder of the small intestine marked by chronic intestinal inflammation, villous blunting, and increased intestinal permeability (15). To test for putative EE in our model, we assessed the expression of several markers of small intestine integrity and inflammation and found no difference between CON and MAL animals (fig. S3A). Moreover, we detected no difference in intestinal integrity as assessed by the functional test of fluorescein isothiocyanate-dextran uptake (fig. S3B). In addition, the levels of proinflammatory markers in sera were similar between the experimental groups, except for the levels of granulocyte colony-stimulating factor and interleukin-6, which were both significantly decreased in MAL-fed mice (fig. S3C). Jejunal histology showed that MAL-fed mice had slightly shorter villi and lower crypt depth (fig. S3D), but we did not observe signs of severe villus blunting or tissue destruction, which are common signs of EE (16). Previously, Ueno *et al.* (17) reported a lower number of proliferating cells in the small intestine of stunted mice fed with a low-protein, low-fat diet. Consistent with this, the MAL-fed mice had a lower number of Ki67⁺ cells in ileal crypts compared with CON-fed animals, suggesting a lower renewal rate of the intestinal epithelium during chronic undernutrition (fig. S3E).

The growth factor IGF-1 is the main endocrine determinant of postnatal growth (18, 19), and its production and activity is reduced upon poor nutrition (20). As expected, we

¹Laboratory of Gnotobiology, Institute of Microbiology of the Czech Academy of Sciences, 54922 Nový Hradec, Czech Republic. ²Institut de Génétique Fonctionnelle de Lyon, Ecole Normale Supérieure de Lyon, CNRS UMR5242, UCBL Lyon-1, F-69007 Lyon, France. ³CarMeN Laboratory, INSERM, INRAE, Université Claude Bernard Lyon 1, 69310 Pierre-Bénite, France. ⁴Laboratory of Immunobiology, Institute of Molecular Genetics of the Czech Academy of Sciences, 14220 Prague, Czech Republic. ⁵Univ Lyon, Hospices Civils de Lyon, Gastro-enterology and Pediatric Nutrition, Hôpital Femme Mere Enfant, F-69500 Bron, France. ⁶Université Paris-Saclay, INRAE, AgroParisTech, Micalis Institute, 78350 Jouy-en-Josas, France. ⁷Genomics Core Facility, European Molecular Biology Laboratory, 69117 Heidelberg, Germany. ⁸Institut Pasteur, Université Paris Cité, CNRS UMR6047, INSERM U1306, Biology and Genetics of the Bacterial Cell Wall Unit, F-75015 Paris, France. ⁹University of Lille, Inserm, U1003, F-59000 Lille, France.

*Corresponding author. Email: schwarzer@biomed.cas.cz (M.Sc.); francois.leulier@ens-lyon.fr (F.L.)

†Present address: Department of Molecular and Clinical Medicine/Wallenberg Laboratory, Institute of Medicine, University of Gothenburg and Sahlgrenska University Hospital, 40530 Gothenburg, Sweden.

‡Present address: Bioaster, Institut de Recherche Technologique, 69007 Lyon, France.

§Present address: LVMH Research 185, 45804 Saint Jean de Braye Cedex, France.

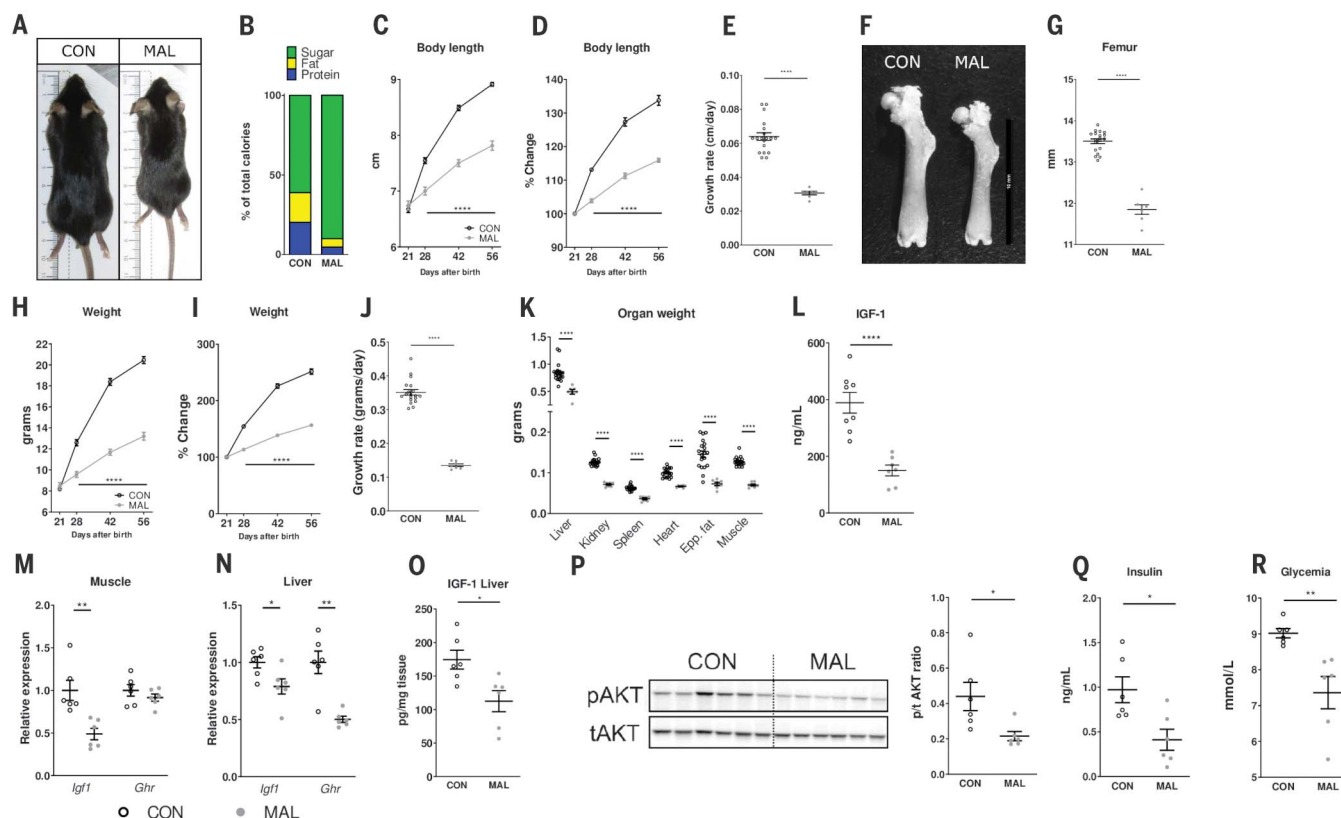


Fig. 1. Feeding a low-protein and low-fat diet induces stunting in C57Bl/6J juvenile male mice. (A) Representative images of C57Bl/6J male mice fed for 35 days after weaning a control diet (CON) or a low-protein, low-fat isocaloric diet (MAL). (B) Schematic of the components of each diet, expressed as a percentage of total calories. (C to G) Body length growth curves (C), relative body length growth curves (D), body length growth rate (E), representative picture of femur bones (F), and quantification of femur bone length (G) at day 56 after birth of mice fed CON (black open circles, $n = 19$) and MAL (gray circles, $n = 7$) diets. (H to K) Weight growth curves (H), relative weight growth curves (I), weight growth rate (J), and organ weight (K) at day 56 after

birth of mice fed CON (black open circles, $n = 19$) and MAL (gray circles, $n = 7$) diets. (L) IGF-1 levels in sera of CON (black open circles, $n = 8$) and MAL (gray circles, $n = 7$) mice at day 56 after birth. (M and N) Expression levels of *Igf1* and *Ghr* depicted as fold change relative to the CON-fed mice in muscle (M) and liver (N) at day 56 after birth. (O) IGF-1 levels in liver tissues. (P) Western blots and quantification of phospho-S473-Akt in liver of CON- and MAL-fed mice. (Q and R) Insulin levels in sera of CON- and MAL-fed mice (Q) and glycemia (R) at day 56 after birth. CON, $n = 6$; MAL, $n = 6$. Data are presented as mean \pm SEM and dot plots with mean \pm SEM. Unpaired Student's *t* test, * $P < 0.05$, ** $P < 0.01$, **** $P < 0.0001$.

found lower levels of circulating IGF-1 in the sera of MAL-fed animals (Fig. 1L). Concomitantly, *Igf1* expression was reduced both in the muscle and liver of MAL-fed animals (Fig. 1, M and N). The production of IGF-1 in peripheral tissues is activated by GH signaling (1). We found that GH receptor expression was significantly lower in the liver of stunted mice (Fig. 1N). The liver is the main source of circulating IGF-1 (21). Consistent with the increased *Igf1* expression, the IGF-1 content per milligram of liver tissue was higher in CON-fed animals (Fig. 1O). This result, together with the higher weight of liver tissues in CON animals (Fig. 1K), indicates that the liver of CON mice produced a significantly higher total amount of IGF-1. Next, we assessed the signaling activity of the insulin receptors (InRs) and IGF-1 receptors (IGF-1Rs) in the liver. The phosphorylation of Akt at Ser⁴⁷³ (phospho-S473-Akt), a marker of both

InR and IGF-1R signaling (22), was reduced in the liver of MAL-fed animals compared with the CON group (Fig. 1P). Insulin is another potent anabolic hormone with growth-promoting properties (23). Insulin levels are decreased during protein malnutrition in humans (24) and in animal models (25). We found that MAL animals had significantly lower circulating levels of both insulin and glucose after fasting compared with the CON group (Fig. 1, Q to R). Taken together, our results establish a new preclinical model of mouse chronic undernutrition resulting in severe stunting associated with low levels of IGF-1 and insulin and low signaling activity of the somatotropic axis with no signs of EE.

Lp^{WJL} treatment improves systemic growth

Previously, we have shown that the *Lp^{WJL}* strain sustains the growth and development of *Dro-*

sophila juveniles upon nutrient scarcity (13). This strain-specific growth-promoting property is also observed in a monoxenic mouse models during chronic undernutrition (10). We now wanted to test whether the *Lp^{WJL}* strain retains its beneficial effects on juvenile growth in the context of a malnourished conventional mouse model. To this end, male mice were weaned on the MAL diet and regularly administered 2×10^8 colony-forming units (CFU) of live *Lp^{WJL}* or a placebo for 5 weeks (Fig. 2A). Administration of *Lp^{WJL}* alone without improved nutrition supported body and femur length (Fig. 2, B to E) and weight gains (Fig. 2, G and H), resulting in animals that were 3.5% longer and 10% heavier at 8 weeks of age compared with the placebo group (Fig. 2, F and J). *Lp^{WJL}* administration resulted in longer femur bones (Fig. 2E) and increased mass of kidney, epididymal fat, and muscle

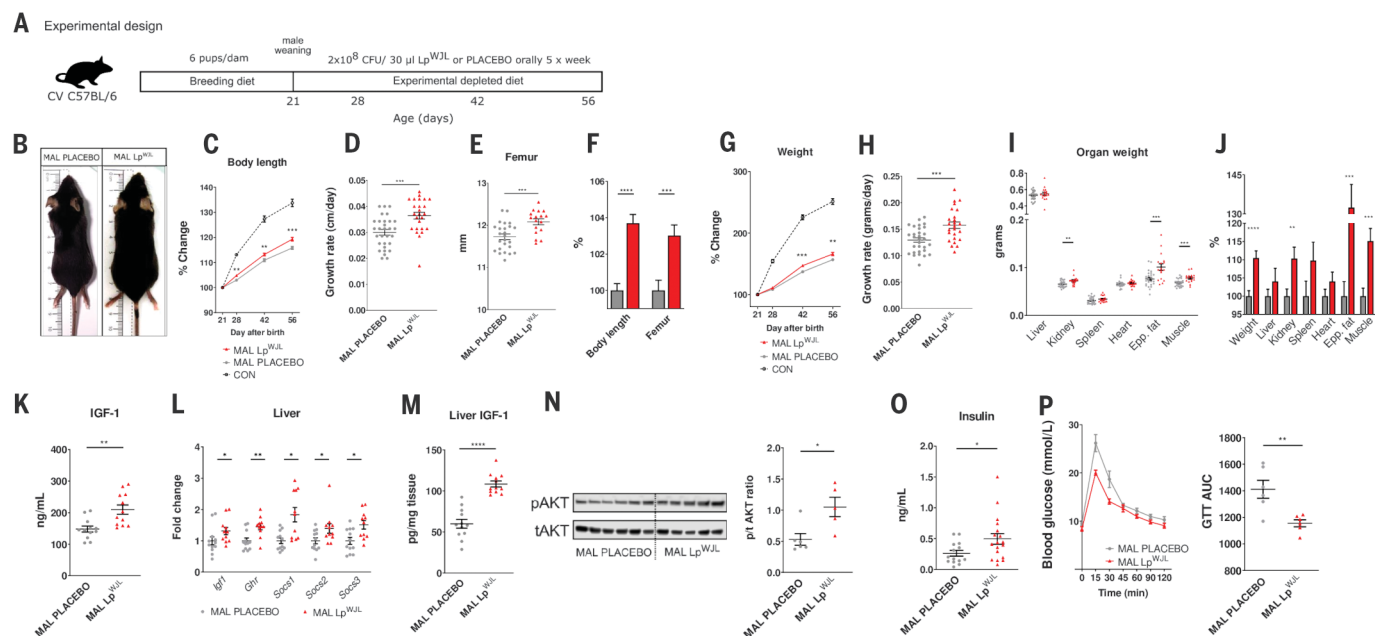


Fig. 2. Lp^{WJL} treatment improves postweaning growth, increases IGF-1/insulin levels, and improves glucose metabolism in undernourished C57BL/6J juvenile male mice. (A) Experimental design. (B) Representative images of 56-day-old MAL-fed C57BL/6J male mice treated either with placebo (MAL PLACEBO) or with Lp^{WJL} (MAL Lp^{WJL}). (C and D) Relative body length growth curves (C) and body length growth rate (D) of MAL-fed mice treated with placebo (gray circles, $n = 30$) and Lp^{WJL} (red triangles, $n = 26$). (E) Quantification of femur bone length at day 56 after birth after treatment with placebo (gray circles, $n = 27$) and Lp^{WJL} (red triangles, $n = 17$). (F) Percentage body and femur bone length gain after Lp^{WJL} treatment compared with placebo. (G and H) Relative weight growth curves (G) and weight growth rate (H) of MAL-fed mice treated with placebo (gray circles, $n = 30$) and Lp^{WJL} (red triangles, $n = 26$). Black open circles, dotted line in (C) and (G) are CON males from Fig. 1 for comparison, $n = 19$. (I) Organ weight at day 56 after birth

of MAL-fed mice treated with placebo (gray) ($n = 27$) and Lp^{WJL} (red) ($n = 17$). (J) Percentage weight and organ weight gain after Lp^{WJL} treatment compared with placebo. (K) IGF-1 levels in sera of placebo (gray) and Lp^{WJL} (red) MAL-fed mice. (L) Expression levels of *Igf1*, *Ghr*, and *Socs* genes depicted as fold change relative to the placebo-treated mice in liver. (M) IGF-1 levels in liver tissues at day 56 after birth. MAL PLACEBO, $n = 12$; MAL Lp^{WJL} , $n = 12$. (N) Representative Western blots and quantification of phospho-S473-Akt in liver of MAL placebo-treated ($n = 6$) and MAL Lp^{WJL} -treated ($n = 5$) mice. (O) Insulin levels in sera of MAL placebo-treated ($n = 14$) and MAL Lp^{WJL} -treated ($n = 18$) mice at day 56 after birth. (P) Intraperitoneal glucose tolerance test (2 g/kg) of MAL placebo-treated ($n = 6$) and MAL Lp^{WJL} -treated ($n = 6$) mice at day 50 after birth. Data are presented as mean \pm SEM and dot plots with mean \pm SEM. Unpaired Student's *t* test, * $P < 0.05$, ** $P < 0.01$, *** $P < 0.001$, **** $P < 0.0001$.

tissues after 5 weeks of treatment at postnatal day 56 (Fig. 2I). These observed postweaning growth differences were not a result of an alteration in the food intake or relative food intake between Lp^{WJL} and placebo groups (fig. S4, A to E). Similar results were obtained in BALB/c male mice, suggesting that improved growth was not specific to the C57BL/6J mouse genetic background (fig. S5, A to D). To test the possibility that the placebo-treated mice were only delayed in growth and would catch up later in life, we extended the treatment for 4 more weeks. At postnatal day 84, we still observed significant differences in body and femur length between placebo- and Lp^{WJL} -treated male mice on the MAL diet (fig. S6, A to C). We next sought to determine the changes induced by Lp^{WJL} treatment on the IGF-1 and insulin circulating levels and related signaling pathways in MAL-fed mice. We found significantly increased levels of IGF-1 in the sera of Lp^{WJL} -treated mice compared with the placebo group (Fig. 2K). The relative

expressions of *Igf1* and *Ghr* were also increased in the liver, suggesting a higher GH sensitivity (Fig. 2L). This was further supported by increased expression of the GH signaling pathway transcriptional target genes *Socs1*, *Socs2*, and *Socs3* (Fig. 2L) and the higher IGF-1 content per milligram of liver tissue in the Lp^{WJL} -treated animals (Fig. 2M). In Lp^{WJL} -treated mice, we detected significantly increased phosphorylation of Akt at Ser⁴⁷³ in the liver (Fig. 2N), which was accompanied by increased levels of fasting insulin in the sera, suggesting higher activity of the InR/IGF-1R pathway in these animals (Fig. 2O). Accordingly, blood glucose control was improved by Lp^{WJL} treatment, as reflected by a faster glucose clearance after intraperitoneal glucose injection (Fig. 2P). These data align with a recent clinical study in which the authors reported a significant increase in the levels of both IGF-1 and insulin in severe acute malnourished Bangladeshi children who received microbiota-directed therapeutic food treatment (8).

Exploring whether the effects of Lp^{WJL} treatment are sex specific, we found that both male and female Lp^{WJL} -treated mice on the MAL diet had significantly improved body and femur length compared with placebo-treated animals (fig. S7, A to C and H to J). We found no differences in fed or fasted glycemia, and the levels of fed and fasted IGF-1 were significantly increased in Lp^{WJL} -treated animals of both sexes (fig. S7, D, E, K, and L). There were no differences in fed insulin levels for either sex (fig. S7, F and M). Consistent with our previous results, Lp^{WJL} -treated male mice had increased fasted insulin levels compared with placebo controls (fig. S7F). Conversely, Lp^{WJL} -treated females had decreased fasted insulin levels (fig. S7M), suggesting that IGF-1 is the main endocrine driver of growth in both sexes. Both male and female Lp^{WJL} -treated mice had improved blood glucose control with significantly lower area under the curve values after glucose injection (fig. S7, G and N). Collectively, our results show that Lp^{WJL} treatment

sensitizes the somatotrophic axis and supports IGF-1 and insulin signaling, which together improved the metabolic status of the malnourished juvenile mice and consequently improved systemic growth and promoted weight gain.

The growth-promoting effects of Lp^{WJL} are strain specific

Using *Drosophila* and mouse monoxenic models, we previously showed that the growth-promoting properties of *L. plantarum* are strain specific. Despite similar intestinal tract colonization abilities, Lp^{WJL} is a marked growth promoter, whereas other *L. plantarum* strains, including NIZO2877 ($Lp^{NIZO2877}$), show a milder effect (10). To determine whether this strain specificity also holds true in conventional mice, we administered 2×10^8 CFU of either live Lp^{WJL} or live $Lp^{NIZO2877}$ to male mice weaned on the MAL diet and monitored their juvenile growth. Similar to the placebo treatment, and in contrast to Lp^{WJL} , the administration of the $Lp^{NIZO2877}$ had no impact on length and femur growth (Fig. 3, A to C), confirming that the growth benefit depends on the *L. plantarum* strain used. We also observed that Lp^{WJL} and $Lp^{NIZO2877}$ differed in their ability to sustain IGF-1 and insulin levels in sera. Levels in $Lp^{NIZO2877}$ -treated animals resembled those of placebo-treated animals (Fig. 3, D and E). $Lp^{NIZO2877}$ treatment had no impact on the blood glucose control of mice on the MAL diet, as reflected by glucose clearance during a glucose tolerance test (Fig. 3F). These data establish that the growth-promoting property of *L. plantarum* in malnourished conventional animals is strain specific. This strain specificity indicates that a biological interaction occurs between Lp^{WJL} and host cells to establish a molecular dialogue supporting systemic growth.

Lp^{WJL} isolated cell walls are sufficient to promote growth

Bacterial cell walls (CW) are a major source of molecular determinants shaping the host-microbe interaction (26–28). Previously, we found in a *Drosophila* model that sensing of *L. plantarum* CW fragments by the host plays an important role in *L. plantarum*-mediated growth promotion under nutrient scarcity (29, 30). This prompted us to test the hypothesis that host sensing of bacterial CW underscores the Lp^{WJL} growth-promoting capability in mice. First, we treated the MAL-fed male mice with 2×10^8 CFU of heat-killed (HK) Lp^{WJL} . HK Lp^{WJL} administration significantly improved the length growth rate of the mice (Fig. 3, G and H), and their femur length was also significantly longer compared with the placebo-treated group (Fig. 3I). Similar to live Lp^{WJL} treatment, the treatment with HK bacteria led to an increase of IGF-1 and

insulin levels in sera (Fig. 3, J and K) and lower blood glucose during a glucose tolerance test (Fig. 3L).

Encouraged by these results and to further explore the role of the bacteria CW, we isolated the CW from Lp^{WJL} or $Lp^{NIZO2877}$ and treated the MAL-fed male mice with CW amounts corresponding to the CW amounts purified from 2×10^8 CFU cells. Lp^{WJL} CW treatments significantly improved the length growth rates of the juvenile mice (Fig. 3, G and H) and increased their femur length compared with the placebo-treated group (Fig. 3I). In stark contrast, treatment with $Lp^{NIZO2877}$ CW had no significant effect on the length growth rates (Fig. 3, G and H), and the mice resembled the placebo-treated group in physical traits. Treatment with Lp^{WJL} CW led to an increase of IGF-1 and insulin levels in sera, whereas treatment with $Lp^{NIZO2877}$ CW had no effect on these parameters (Fig. 3, J and K). Similar to when mice were treated with live Lp^{WJL} cells, the Lp^{WJL} CW treatment led to lower blood glucose during a glucose tolerance test (Fig. 3L). Feeding with $Lp^{NIZO2877}$ CW failed to significantly decrease the area under the curve after the glucose challenge (Fig. 3L). These data demonstrate that HK

Lp^{WJL} and, more specifically, Lp^{WJL} isolated CW, are sufficient to support improved growth and glucose metabolism during chronic undernutrition.

NOD2 is necessary for Lp^{WJL} -mediated growth promotion

Our results suggest that HK Lp^{WJL} and isolated CW from Lp^{WJL} can be sensed by the host and induce metabolic and hormonal changes, leading to improved growth kinetics during chronic undernutrition. To identify such host-sensing and signaling mechanism(s), we tested the signaling potential of HK strains and their CW in human embryonic kidney (HEK) cells stably transfected with a set of innate immune receptors previously reported to sense molecular determinants from bacteria CW (NOD1, NOD2, TLR2, and TLR4) (31, 32). We observed that HK Lp^{WJL} signaling through the NOD2 receptor was increased compared with HK $Lp^{NIZO2877}$. Signaling of both HK strains through the TLR2 receptor was comparable (fig. S8A). Similarly to HK bacterial strains, Lp^{WJL} CW signaling through the NOD2 receptor was significantly increased compared with the $Lp^{NIZO2877}$ CW. By contrast, $Lp^{NIZO2877}$ CW signaling through the TLR2 receptor was

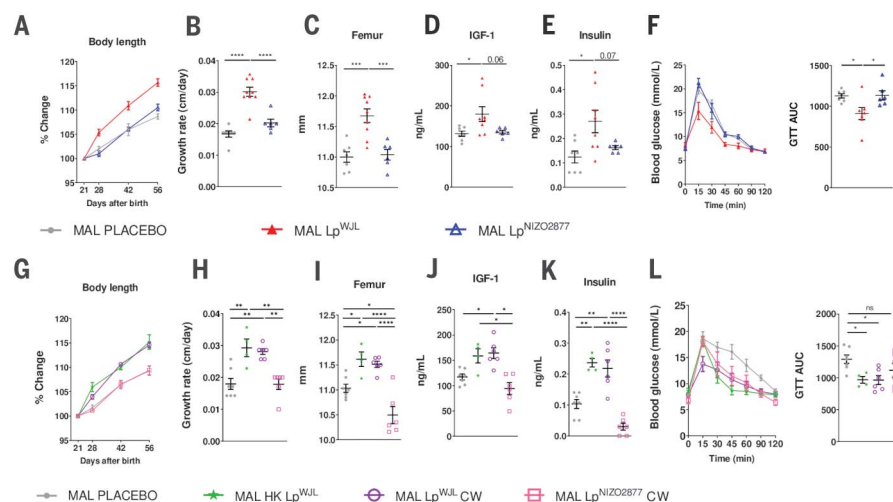


Fig. 3. The growth-promoting and metabolic effects of Lp^{WJL} are strain specific and can be replicated by HK Lp^{WJL} or Lp^{WJL} isolated CW. (A to C) Relative body length growth curves (A), body length growth rate (B), and femur length (C) at day 56 after birth of placebo-treated (MAL PLACEBO, gray circles, $n = 7$), Lp^{WJL} -treated (MAL Lp^{WJL} , red triangles, $n = 9$), and $Lp^{NIZO2877}$ -treated (MAL $Lp^{NIZO2877}$, blue open triangles, $n = 6$) MAL-fed mice. (D and E) IGF-1 (D) and insulin (E) levels in sera of placebo-treated (gray circles, $n = 7$), Lp^{WJL} -treated (red triangles, $n = 8$), and $Lp^{NIZO2877}$ -treated (blue open triangles, $n = 6$) MAL-fed mice at day 56 after birth. (F) Intra-peritoneal glucose tolerance test (2 g/kg) of placebo-treated (gray circles, $n = 7$), Lp^{WJL} -treated (red triangles, $n = 7$), and $Lp^{NIZO2877}$ -treated (blue open triangles, $n = 6$) MAL-fed mice at day 50 after birth. (G to K) Relative body length growth curves (G), body length growth rate (H), femur length (I), IGF-1 (J), and insulin levels (K) in sera at day 56 after birth. (L) Intra-peritoneal glucose tolerance test (2 g/kg) at day 50 after birth in placebo-treated (gray circles, $n = 7$), HK Lp^{WJL} -treated (MAL HK Lp^{WJL} , green stars, $n = 4$), Lp^{WJL} CW-treated (MAL Lp^{WJL} CW, purple open circles, $n = 6$), and $Lp^{NIZO2877}$ -treated (MAL $Lp^{NIZO2877}$ CW, pink open squares, $n = 6$) MAL-fed mice. Data are presented as mean \pm SEM and dot plots with mean \pm SEM. ANOVA with Tukey's multiple-comparisons test, * $P < 0.05$, ** $P < 0.01$, *** $P < 0.001$, **** $P < 0.0001$.

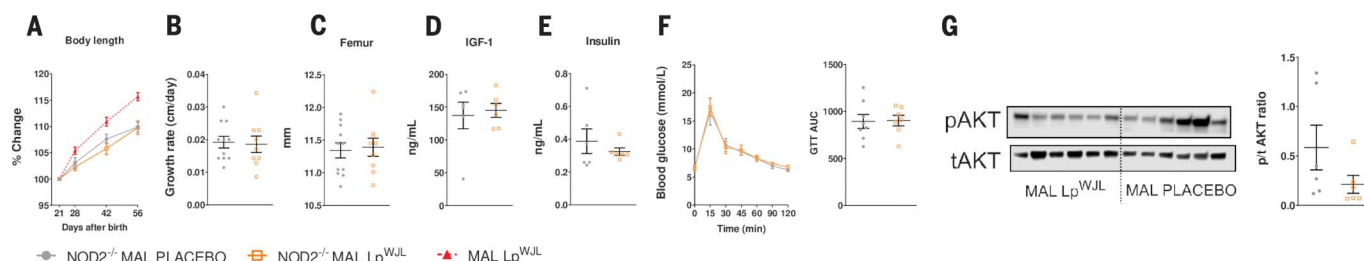


Fig. 4. NOD2 sensing is necessary for Lp^{WJL}-mediated growth-promoting and metabolic effects. (A to C) Relative body length growth curves (A), body length growth rate (B), and femur length (C) of placebo-treated (gray circles, $n = 11$) and Lp^{WJL}-treated (orange open squares, $n = 9$) MAL-fed NOD2 KO mice. Red triangles, dotted line in (A) are MAL Lp^{WJL} males from Fig. 3 for comparison, $n = 9$. (D and E) IGF-1 (D) and insulin (E) levels in sera of placebo-treated (gray circles, $n = 6$) and Lp^{WJL}-treated (orange open squares,

$n = 6$) MAL-fed NOD2 KO mice at day 56 after birth. (F) Intraperitoneal glucose tolerance test (2 g/kg) of placebo-treated (gray circles, $n = 8$) and Lp^{WJL}-treated (orange open squares, $n = 7$) MAL-fed NOD KO mice at day 50 after birth. (G) Representative Western blots and quantification of phospho-S473-Akt in liver of NOD2 KO MAL placebo-treated (gray circles, $n = 6$) and MAL Lp^{WJL}-treated (orange open squares, $n = 6$) mice. Data are presented as mean \pm SEM and dot plots with mean \pm SEM, unpaired Student's t test.

increased compared with Lp^{WJL} CW (fig. S8A). Neither HK bacteria nor the isolated CW were able to signal through the NOD1 or TLR4 receptor in this assay (fig. S8A). Peptidoglycans (PGs) are the major CW component of Gram-positive bacteria (26). We therefore extracted and analyzed the composition of the PGs from the two strains. We found no differences in mucopeptide composition and only subtle differences in meso-diaminopimelic acid amidation and sugar acetylation of specific mucopeptides (fig. S8B and table S2). When tested in the NOD2 HEK cell system, the isolated PGs from each strain or their mutanolysin digests did not elicit any differences in NOD2 signaling (fig. S8C). Therefore, these results indicate that the observed strain specificity does not stem from variation in PG structure but rather from physiological attributes of the individual strains. This could be the differential ability of shedding CW fragments in the intestine or additional strain-specific molecular determinants in the bacterial cell envelope, such as D-alanylation of teichoic acids, which we have shown to be an important Lp CW feature shaping *Drosophila* growth (30).

To test the possible importance of NOD2-mediated Lp^{WJL} recognition in the growth promotion and improvement of the metabolic status of undernourished mice in vivo, we used Nod2-deficient (Nod2^{-/-}) mice and, as a control, mice deficient in the MyD88 cytoplasmic adapter molecule (MyD88^{-/-}) essential for the signaling of several TLRs (33). First, we confirmed that these two knockout (KO) mice models responded to the MAL diet similarly to C57Bl/6J mice in terms of growth phenotypes. In both genetic contexts, male mice were stunted and showed low levels of IGF-1 in sera when weaned on the MAL diet compared with the CON-fed animals (fig. S9, A and B). Next, we assessed the impact of Lp^{WJL} treatment in

these genetic contexts. We found that Nod2^{-/-} male mice failed to benefit from the Lp^{WJL} treatment, as shown by the absence of length gains (Fig. 4, A and B) and the lack of femur size gain compared with the placebo-treated group (Fig. 4C). Concomitantly, Lp^{WJL}-treated Nod2^{-/-} mice had similar fasted levels of IGF-1 and insulin in sera (Fig. 4, D and E), and their glucose tolerance was unchanged compared with placebo-treated MAL-fed mice (Fig. 4F). Finally, there was no difference in phosphorylation of Akt at Ser⁴⁷³ in liver (Fig. 4G). In contrast to Nod2^{-/-} mice, undernourished MyD88^{-/-} male mice still benefited from Lp^{WJL} administration, as demonstrated by significantly higher length growth rates (fig. S10, A and B), significantly increased fasted IGF-1 in sera (fig. S10C), and faster glucose clearance compared with the MyD88^{-/-} placebo-treated mice (fig. S10D).

Having established that NOD2 is necessary for the Lp^{WJL}-mediated growth-promoting and metabolic effects, we wondered whether treatment of mice with synthetic NOD2-activating derivatives, such as bacterial CW-derived muramyl dipeptide (MDP) or synthetic NOD2-activating adjuvant mifamurtide (muramyl tripeptide phosphatidylethanolamine) (34), would be able to improve juvenile growth during undernutrition. We treated male mice orally with 25 μ g of MDP dissolved in placebo or an isomolar amount of 62.5 μ g of mifamurtide dissolved in dimethyl sulfoxide (DMSO)/placebo. We observed that the length gains and final femur length of MDP-treated mice was improved compared with placebo, but not to the extent of Lp^{WJL}-treated mice (fig. S11, A to C). MDP treatment increased the levels of IGF-1 compared with placebo (fig. S11D), but failed to increase the insulin levels or the glucose clearance after glucose injection (fig. S11, E and F). We observed a similar growth-promoting effect after mifamurtide treat-

ment, with increases in both IGF-1 and insulin (fig. S11, G to K). Again, there was no difference in glucose clearance after glucose injection compared with the DMSO/placebo-treated controls (fig. S11L). These results establish that NOD2 sensing and signaling is necessary for the Lp^{WJL}-mediated growth-promoting and metabolic effects, and that synthetic NOD2 ligands can partially mimic the Lp^{WJL} effects.

NOD2 is necessary for the Lp^{WJL}-mediated increase in Ki67⁺ cell numbers in the small intestine

We initially observed that the MAL-fed mice had lower number of Ki67⁺ cells in small intestinal crypts compared with CON-fed animals (fig. S3E), which suggested a lower renewal rate of the intestinal epithelium and altered function of intestinal stem cells (ISCs) during chronic undernutrition (35). It was previously reported that NOD2 stimulation in the small intestine crypt contributes to ISC survival and function (36). In the light of our results establishing that NOD2 is a key sensor supporting the increased growth after Lp^{WJL} treatment, we analyzed the jejunum of Lp^{WJL}- and placebo-treated mice and observed increased numbers of Ki67⁺ cells per intestinal crypt in Lp^{WJL}-treated mice compared with the placebo group (Fig. 5A). This phenomenon was reminiscent of *Lactocaseibacillus rhamnosus*-mediated cell proliferation in the small intestine crypts previously reported by Jones *et al.* (37). Further, we performed a transcriptome analysis by RNA sequencing of the whole jejunal tissue of Lp^{WJL}- and placebo-treated mice, and found that many up-regulated genes in Lp^{WJL}-treated animals were genes responding to type I interferon (IFN) (Fig. 5, B and C). A positive correlation between fecal IFN- β and the rate of weight gain has been recently reported after treatment of severely acutely malnourished Bangladeshi children

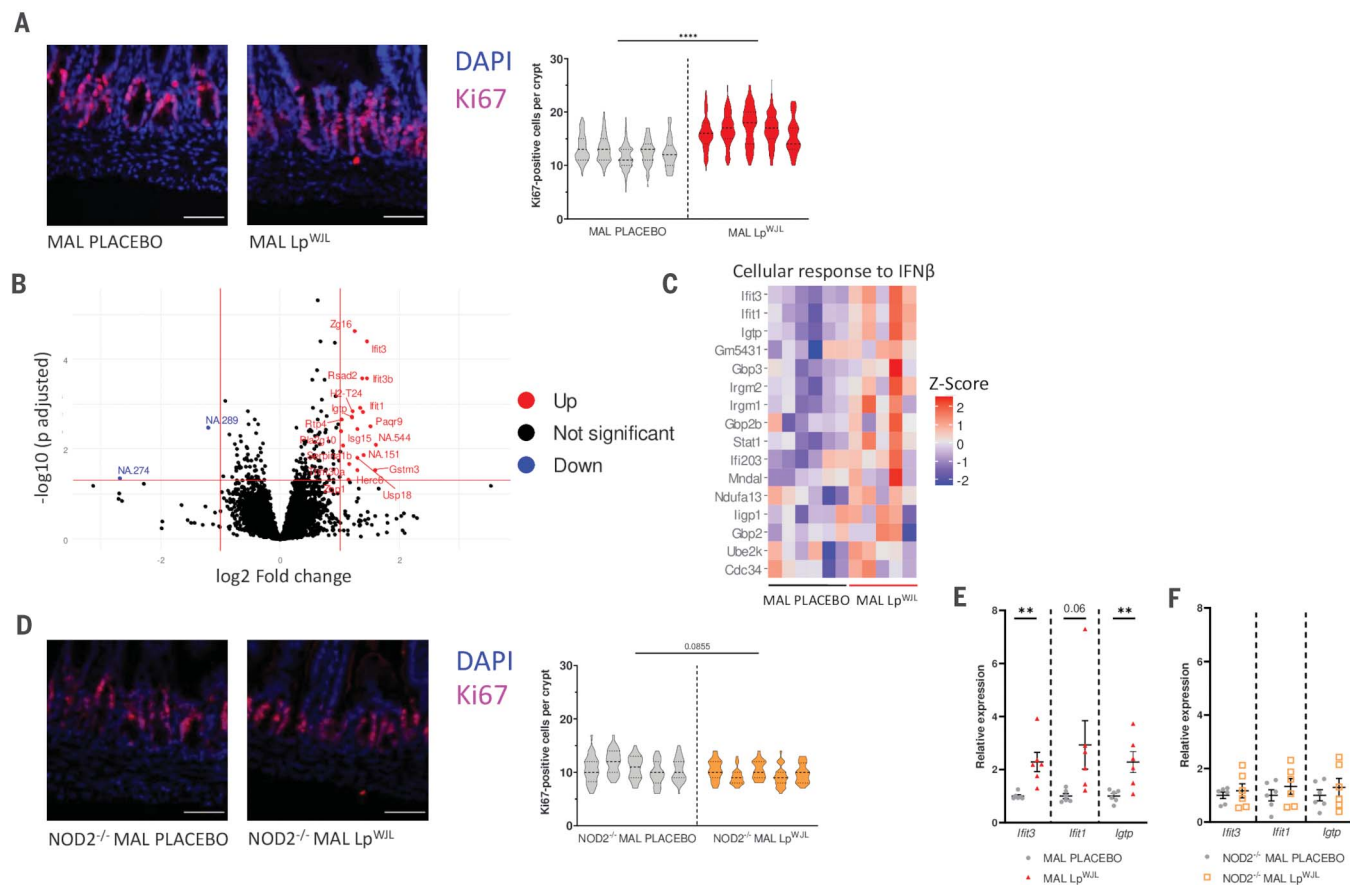


Fig. 5. NOD2-dependent Lp^{WJL} sensing increases the number of Ki67⁺ cells and expression of type I IFN response genes in the small intestine.

(A) Representative images of Ki67 staining in the jejunum of MAL-fed C57Bl/6J male mice and quantification of Ki67⁺ cells/crypt ($n = 5$ mice/group). Scale bar, 50 μ m. Each violin plot represents a single mouse with minimum of 24 crypts/mouse counted. (B) RNA-seq analysis of pathways changed in jejunum of Lp^{WJL}-treated ($n = 5$) MAL-fed C57Bl/6J male mice compared with placebo ($n = 6$). DESeq2 calculated log fold changes were used as input and analyzed for enrichment of pathways using the Gene Ontology (GO) resource. (C) Heatmap of the most changed genes from the cellular response to IFN β gene set showing values of individual samples. (D) Representative images of Ki67 staining in the

jejunum of MAL-fed NOD2 KO male mice and quantification of Ki67⁺ cells/crypt ($n = 5$ mice/group). Scale bar, 50 μ m. Each violin plot represents a single mouse with 20 to 34 crypts/mouse counted. (E) Expression levels of *Ifit3*, *Ifit1*, and *Igtp* genes in the jejunum of MAL-fed C57Bl/6J male mice depicted as fold change relative to the placebo-treated (gray circles, $n = 6$) and Lp^{WJL}-treated (red triangles, $n = 6$) mice. (F) Expression levels of *Ifit3*, *Ifit1*, and *Igtp* genes in the jejunum of MAL-fed NOD2 KO male mice depicted as fold change relative to the placebo-treated (gray circles, $n = 6$) and Lp^{WJL}-treated (orange open squares, $n = 6$) mice. Data are presented as violin plots and dot plots with mean \pm SEM. Data in (A) and (D) were analyzed by nested t test. Data in (E) and (F) were analyzed by unpaired Student's t test, ** $P < 0.01$, *** $P < 0.0001$.

with a Gram-positive *B. infantis* probiotic strain (38). Stimulation of NOD2 has been shown to induce the type I IFN response (39), and concomitantly, type I IFNs play an important role in the stimulation of intestinal epithelial homeostasis (40). These results prompted us to investigate the expression of the Ki67⁺ marker in the intestinal crypt of NOD2^{-/-} mice. We found no significant difference in the number of Ki67⁺ cells between the jejunal crypts of Lp^{WJL}- and placebo-treated mice (Fig. 5D). Furthermore, we examined the expression of three genes, *Ifit3*, *Ifit1*, and *Igtp*, that were up-regulated by Lp^{WJL} treatment in wild-type MAL-fed animals (Fig. 5E) and found no difference between the Lp^{WJL}- and placebo-treated groups of NOD2^{-/-} mice (Fig.

5F). These data further confirm the key role of NOD2 in the recognition and signaling of orally administered Lp^{WJL}.

Intestinal NOD2 is necessary for Lp^{WJL}-mediated growth promotion

The observed changes in the small intestine after Lp^{WJL} treatment in WT and NOD2^{-/-} mice suggested that sensing by NOD2 in the intestinal crypt might be the key for the Lp^{WJL}-induced improved growth kinetics during chronic undernutrition. Conversely, given the central role of the GH/IGF-1 axis activity in the liver during the systemic response triggered by Lp^{WJL}, we could not exclude the possibility that, as previously reported in the context of obesity and fatty liver disease (34, 41), NOD2

is required within hepatocytes to regulate endocrine signals in response to infiltrating PG fragments. To test these hypotheses, we used tissue-specific NOD2 KO strategies. First, we used a transgenic mouse model with an intestinal epithelial cell (IEC)-specific Cre driver Villi-iCre construct encoding a tamoxifen-inducible Cre recombinase (42) (fig. S12A). We crossed Villi-iCre mice to a Rosa26-fl-STOP-fl-TdTomato reporter mouse strain and analyzed the intestinal compartment by flow cytometry (fig. S12B) and fluorescence microscopy (fig. S12C). We confirmed that Villi-iCre is expressed and recombined in the IEC compartment [including the ISC compartment, as previously reported (42)]. Next, we crossed the Villi-iCre to the NOD2^{fl/fl} (fig. S12A) strain, which led to

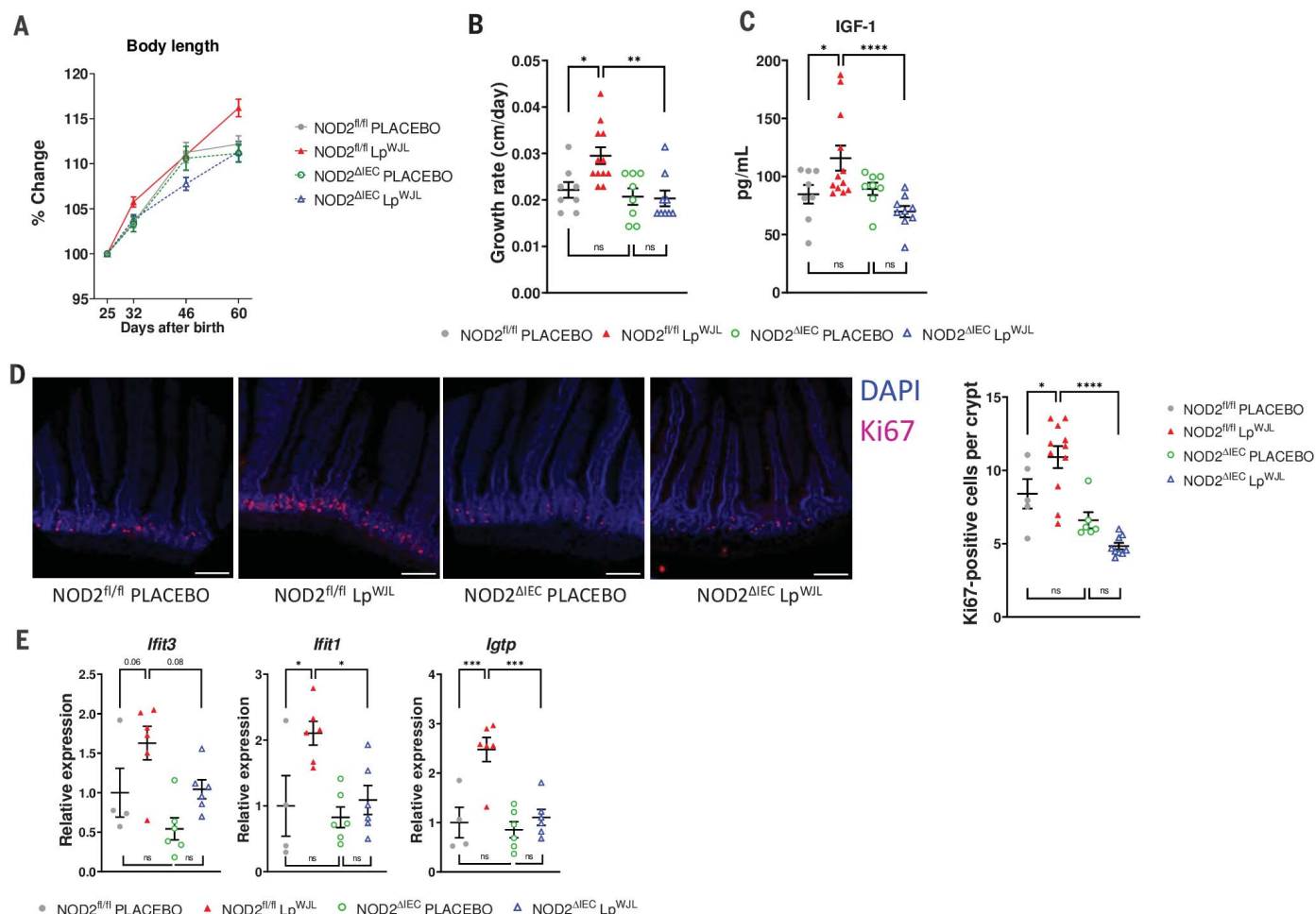


Fig. 6. NOD2-dependent sensing of Lp^{WJL} in the intestinal epithelial compartment is necessary to support juvenile growth during chronic undernutrition.

(A to C) Relative body length growth curves (A), body length growth rate (B), and IGF-1 levels (C) in sera at day 60 after birth of NOD2^{fl/fl} placebo-treated (gray circles, $n = 8$), NOD2 ^{Δ IEC} placebo-treated (green open circles, $n = 8$), NOD2^{fl/fl} Lp^{WJL}-treated (red triangles, $n = 12$), and NOD2 ^{Δ IEC} Lp^{WJL}-treated (blue open triangles, $n = 9$) MAL-fed mice. (D) Representative images of Ki67 staining in the jejunum of NOD2^{fl/fl} placebo-treated (gray circles, $n = 5$), NOD2 ^{Δ IEC} placebo-treated (green open circles, $n = 6$), NOD2^{fl/fl} Lp^{WJL}-treated (red triangles, $n = 11$), and

NOD2 ^{Δ IEC} Lp^{WJL}-treated (blue open triangles, $n = 9$) MAL-fed mice. Scale bar, 100 μ m. Each dot represents a mean of 33 to 57 crypts/mouse counted.

(E) Expression levels of *Ifit3*, *Ifit1*, and *Igtp* genes in the jejunum of NOD2^{fl/fl} placebo-treated (gray circles, $n = 4$), NOD2 ^{Δ IEC} placebo-treated (green open circles, $n = 6$), NOD2^{fl/fl} Lp^{WJL}-treated (red triangles, $n = 6$), and NOD2 ^{Δ IEC} Lp^{WJL}-treated (blue open triangles, $n = 6$) MAL-fed mice. Data are depicted as fold change relative to the NOD2^{fl/fl} placebo-treated mice. Data are presented as dot plots with mean \pm SEM. Data were tested by two-way ANOVA to compare between genotypes and treatments, * $P < 0.05$, ** $P < 0.01$, *** $P < 0.001$, **** $P < 0.0001$.

the IEC-specific Cre-driven genetic depletion of NOD2 (NOD2 ^{Δ IEC}) (fig. S12B). We weaned the male NOD2 ^{Δ IEC} and their NOD2^{fl/fl} male littermates on a MAL diet and treated them with Lp^{WJL} or placebo for 5 weeks. Lp^{WJL}-treated NOD2^{fl/fl} mice showed improved length growth rate compared with Lp^{WJL}-treated NOD2 ^{Δ IEC} mice and the NOD2^{fl/fl} placebo-treated group (Fig. 6, A and B). Concomitantly, there was no length growth difference between the placebo- and Lp^{WJL}-treated NOD2 ^{Δ IEC} groups (Fig. 6, A and B). The increased growth was accompanied by increased IGF-1 in Lp^{WJL}-treated NOD2^{fl/fl} mice compared with Lp^{WJL}-treated NOD2 ^{Δ IEC} and NOD2^{fl/fl} placebo-treated animals (Fig. 6C). Lp^{WJL}-treated NOD2^{fl/fl} mice had also significantly higher numbers of Ki67⁺ cells in the intestinal crypts and increased expression of

type I IFN response genes compared with all other groups (Fig. 6, D and E). These results establish that NOD2 is required in the intestinal epithelium compartment to support Lp^{WJL}-mediated intestinal response and growth promotion.

To explore the possible role of NOD2 within hepatocytes, we used a transgenic hepatocyte-specific constitutive Cre driver [Alb-Cre (21)] to selectively knock out the *Nod2* gene in hepatocytes (fig. S12A). We first verified the specificity of the driver with the Rosa26-fl-STOP-fl-TdTomato reporter mouse strain (fig. S12H) and crossed the Alb-Cre to NOD2^{fl/fl} strain (NOD2 ^{Δ Hep}), which led to the hepatocyte-specific Cre-driven genetic depletion of NOD2 (fig. S12A). We weaned the male NOD2 ^{Δ Hep} mice and their NOD2^{fl/fl} male littermates on a MAL

diet and treated them with Lp^{WJL} for 5 weeks. We did not detect any significant differences between length growth rate or in the levels of IGF-1 between the Lp^{WJL}-treated NOD2^{fl/fl} and the NOD2 ^{Δ Hep} groups (fig. S13, A to C). Therefore, these results indicate that NOD2 is not required in hepatocytes to support the growth of Lp^{WJL}-treated mice. These results reinforce the crucial role of the NOD2 in the intestinal epithelial compartment to support Lp^{WJL}-mediated juvenile growth promotion during chronic undernutrition.

Conclusion

Our results establish that treatment with the bacterial strain Lp^{WJL} or its CW supports the postnatal growth of chronically undernourished juvenile mice by orchestrating metabolic and

hormonal changes in the juvenile host, which are manifested as improved circulating levels of IGF-1 and insulin. The ability of purified CW to support growth, together with the strain specificity of the bacteria-mediated growth promotion phenotypes, point to an important role of the host machinery involved in the sensing of bacterial CW to alleviate stunting upon chronic undernutrition. Consistent with this hypothesis, we demonstrate that NOD2, a key host sensor of bacterial CW, is necessary for Lp^{WJL}-mediated growth promotion, and that NOD2 ligands are sufficient to support improved growth. Specifically, we show that Lp^{WJL} NOD2 sensing and signaling supporting growth occur solely in the intestinal epithelium.

NOD2 is an intracellular innate immune sensor expressed in epithelial and immune cells of the intestine, which ensures the maintenance of intestinal inflammatory and immune homeostasis (43–45). NOD2 is also strongly expressed in stem cells of the intestinal crypts (46), where it controls their proliferation and survival in response to bacterial PGs, the main components of Gram-positive bacteria CW (36). This NOD2-dependent ISC phenotype is reminiscent of the increased number of proliferating cells in the small intestinal crypts upon Lp^{WJL} treatment, a feature lost in NOD2^{-/-} mice. Stem cell proliferation in the crypt is the major biological process ensuring homeostasis of the intestinal epithelium, a prerequisite for its absorptive and protective functions (47). Chronic undernutrition diminishes the number of proliferative ISCs (17, 48), resulting in shorter villi and reduced absorptive epithelial cell numbers, which overall results in a decrease of the small intestinal absorptive area and decreased nutrient absorption (17, 48). We therefore posit that one of the mechanisms by which Lp^{WJL} and its CW exert their postnatal growth-promoting properties is by buffering of the deleterious effect of undernutrition on small intestinal crypt cell proliferation through NOD2-dependent bacterial PG sensing. Lp^{WJL}-mediated NOD2 signaling in the crypt improves intestinal cell proliferation and epithelium maturation, and thus nutrient absorption, which would translate into increased activity of the nutrient-sensitive GH/IGF-1/insulin axis and ultimately improve postnatal growth in a systemic manner. However, this presumption requires further experimental testing.

Collectively, our findings establish that NOD2-dependent sensing in the intestinal epithelial compartment of bacterial CW contributes to sustained postnatal growth upon undernutrition. Our results suggest that, coupled with renutrition strategies, supplementation of evidence-based probiotics such as Lp^{WJL} or defined bacteria-derived postbiotics such as Lp^{WJL} CW and/or NOD2 agonists have the

potential to alleviate persistent stunting, one of the long-term sequelae of undernutrition that still affects >149 million children under the age of 5 years in low- and middle-income countries (49).

Materials and Methods

Animals

Institute of Functional Genomics (IGFL), Lyon, France: Specific pathogen free C57Bl/6J and BALB/c breeders (8 to 9 weeks old) were purchased from Envigo (France). After 1 week of acclimatization at the conventional animal room at IGFL, mice were mated and offspring were used for experiments. Mice were kept in Innorack IVC Mouse 3.5 disposable cages (Inovive, USA), exposed to 12:12 hours light-dark cycles, supplied with tap water and fed *ad libitum* RM3 diet (SDS Diets). All experiments were performed in accordance with the European Community Council Directive of September 22, 2010 (2010/63/EU) regarding the protection of animals used for experimental and other scientific purposes. The research project was approved by a local animal care and user committee (C2EA015) and subsequently authorized by the French Ministry of Research (APAFIS#3147-2015112516275348 v6 and APAFIS#11985-2017100609104032 v7). Results depicted in Figs. 1 and 2 and related supplementary figures were generated at IGFL by using 13% cellulose AIN93G diet (CON, Envigo, containing 17.7% of crude protein and 7.2% of fat; table S1) or the experimental diet low in proteins and fats (MAL, Envigo; table S1).

Institute of Microbiology of the Czech Academy of Sciences, Nový Hradec, Czech Republic: Conventional C57Bl/6J were bred in Laboratory of Gnotobiology for more than 10 generations. C57Bl/6J MyD88 KO and Rosa26TdTOMATO (B6;129S6-Gt(Rosa)26Sortm14(CAG-tdTomato)Hze/J) (50) mice were provided by Dr. Dominik Filipp (Institute of Molecular Genetics, Prague, Czech Republic) and C57Bl/6J NOD2 KO mice were a kind gift from Dr. Tomas Hrnčíř (Laboratory of Gnotobiology, Nový Hradec, Czech Republic). NOD2^{fl/fl} C57Bl/6J mice (originally from Dr. P. Rosenstiel, Institute for Clinical Molecular Biology, Christian-Albrechts-University, Kiel, Germany) and Alb-CRE (129Sv.Cg-Speer6-*ps1Tg*(Alb-cre)21Mgn/MdJ) (51) backcrossed four times with the NOD2^{fl/fl} C57Bl/6J strain creating Alb-CRE NOD2^{fl/fl} were provided by Dr. Ivo Gompers-Boneca (Institute Pasteur, Paris, France). Villi-CreERT (B6.Cg-Tg(Vill-cre/ERT2)23Syr/J) (42) NOD2^{fl/fl} mice were provided by Dr. Mathias Chamailard (University of Lille, Lille, France).

Mice were kept in IVC cages (Tecniplast, Italy), exposed to 12:12 hours light-dark cycles, supplied with tap water, and fed *ad libitum* mouse breeding diet V1124-300 (Ssniff Spezialdiäten GmbH) sterile diet (irradiated

~25 kGy, Bioster, Czech Republic). Animal experiments in Laboratory of Gnotobiology were approved by the Committee for Protection and Use of Experimental Animals of the Institute of Microbiology of the Czech Academy of Science (approval ID: 22/2018, 24/2018 and 56/2021). Results depicted in Figs. 3 to 6 and related supplementary figures were generated at Laboratory of Gnotobiology by using sterile 13% cellulose AIN93G diet (CON, Envigo; table S1) and sterile experimental diet low in proteins and fats (MAL, Envigo; table S1), both irradiated ~45 kGy (Bioster, Czech Republic).

Experimental design

Conventional BALB/c, C57Bl/6J, C57Bl/6J NOD2 KO and C57Bl/6J MyD88 KO mice (10–11 weeks old) were mated. After the delivery the litter size was reduced to six offspring per dam and at day 21 male or female mice were weaned either on the 13% cellulose AIN93G diet (CON, Envigo, containing 17.7% of crude protein and 7.2% of fat; table S1) or the experimental diet low in proteins and fats (MAL, Envigo; table S1) and followed regularly until 42, 56, or 84 days after birth.

For intestinal epithelium-specific KO, NOD2^{fl/fl} mice were crossed to a Villi-CreERT NOD2^{fl/fl} line, which allows gene deletion in all epithelial cells of the intestine upon tamoxifen administration. The Cre enzyme was induced by three i.p. injection of 0.1 (0.3 mg total/mice) mg tamoxifen (Merck # 85256 Supelco) dissolved in sunflower oil (2 mg/ml) on days 10, 11 and 12 after birth. Male mice were weaned at day 25 after birth on MAL diet and followed until day 60. For hepatocyte-specific KO, NOD2^{fl/fl} mice were crossed to an Alb-CRE NOD2^{fl/fl}. Male mice were weaned at day 21 after birth on MAL diet and followed until day 56. The tissue specificity of Villi-CreERT and Alb-Cre were verified by crossing them to Rosa26TdTOMATO mice.

Mice weaned on the MAL diet were followed without treatment or treated 5x/week by the placebo or Lp^{WJL} or Lp^{NIZO2877} or heat-killed Lp^{WJL} or Lp^{WJL} purified cell-wall or Lp^{NIZO2877} purified cell-wall. The daily treatment dose corresponded to 2×10^8 CFU/30 µl of solution. Muramyl dipeptide (InvivoGen, USA, # tlr1-mdp) was dissolved in placebo and mice were treated with 25 µg/30 µl 5x/week. Mifamurtide (CliniSciences, France) was dissolved in DMSO (Merck) to obtain 50 µg/µl stock solution. DMSO stock solution was used to create 62.5 µg mifamurtide (equimolar to 25 µg of MDP)/30 µl of placebo and this was administered to mice 5x/week. Control group received DMSO/placebo mixture. All solutions were administered by a pipette onto the tongue of the mouse. Mouse was held until the solution was swallowed.

For the measurement of body length mice were briefly anesthetized by isoflurane (Piramal

Healthcare, UK). Weight was measured twice and the scales (Acculab mini PP201, Sartorius, Germany) were tared between the measurements. Food intake was measured by subtracting the amount of remaining and spilled food pellets from the amount of food provided during the experiment. Food and bedding were removed at 8 a.m. Fed and fasted glucose levels were measured by tail-tip bleeding with glucometer FreeStyle Lite (Abbott, Canada). Mice were sacrificed after 5 hours fasting by isoflurane inhalation and cervical dislocation. All animals were sacrificed within one hour between 1:00 and 2:00 p.m. Heart, spleen, liver, kidney, epididymal adipose tissue, and gastrocnemius muscle were removed and weighed. Liver, gastrocnemius muscle, and sections of small intestine were snap-frozen and stored at -80°C until processing.

Genotyping of NOD2^{fl/fl}, Vill1-Cre, and Alb-Cre mice

Mouse tail tip was cut off and DNA was extracted using the KAPA Mouse Genotyping Kit (Merck, MGKITKB) following the manufacturer's manual. After the quick centrifugation extracted DNA was diluted 10x with 10 mM Tris-HCl (pH 8.0–8.5). Each PCR reaction (20 μl) consisted of 10 μl 2X KAPA2G Fast (HotStart) Genotyping Mix with dye, 2 μl template DNA (10X diluted), 0.5 μM of each forward and reverse primers (table S3). The PCR product was separated on 1.2% agarose (TopBio, P045) gel in 1x ultrapure TAE buffer (Invitrogen, 15558042), stained in ethidium bromide solution and visualized with fluorescent image analyzer (FLA-7000, Fujifilm).

Flow cytometry analysis

Small intestine was dissected, cleaned from mesenteric fat and Peyer's patches were removed. Duodenum, and 6 cm of jejunum and ileum were separated and cut open longitudinally. Tissues were cut to 2 cm long pieces and washed by vigorous shaking in ice-cold PBS to remove luminal contents. Cleaned tissue pieces were incubated twice in HBSS buffer (Merck, H6648) supplemented with 3% FBS and 2mM EDTA for 20 min at 37°C . Remaining tissue was discarded and the buffer containing epithelial cells was collected. Single cell suspension of epithelial cells was obtained by digestion in TrypLE enzyme (Gibco, 12604013) for 1 min at 37°C . Cells were washed with HBSS buffer supplemented with 3% FBS and 2mM EDTA and used for flow cytometry analysis. For the isolation of liver cells, 2-cm portion of liver was dissected and cut to ~2mm pieces. These pieces were incubated in RMPI (Gibco, 21875034) medium supplemented with collagenase D (1 mg/ml, Roche), DNase I (40 U/ml, Roche) and 3% FBS for 1 hour at 37°C . Every 20 min, cell suspension was dislodged from tissue pieces by serial pipetting using cut

tip. Cell suspension was then passed through 100 μm filter, washed with HBSS buffer supplemented with 3% FBS and 2 mM EDTA and used for flow cytometry analysis. Staining was performed in HBSS buffer supplemented with 3% FBS and 2 mM EDTA on ice for 20 min. Intestinal epithelial cells were stained with CD45-FITC (BioLegend, clone 30-F11) and EpCAM-APC (BioLegend, clone G8.8). Liver cells were stained with CD45-FITC (BioLegend, clone 30-F11) and CD31-APC (BioLegend, clone 390). Hoechst 33258 was added directly prior to the analysis to determine cell viability. Samples were analyzed using LSRII or Symphony FACS flow cytometers (both BD Biosciences). Flow cytometry data were analyzed using FlowJO software (v10.8.1, BD Biosciences).

Bacterial strains preparation for mouse treatment

Lp^{WJL}, formally *Lactobacillus*, reclassified based on (52), originally isolated from posterior midgut of adult *Drosophila* (kind gift from Prof. Won Jae Lee, South Korea) was cultured overnight in Man, Rogosa and Sharpe (MRS) medium (Biokar Diagnostics, France) at 37°C without agitation. After centrifugation (20,000g for 60 min, RT) the pellet was dissolved in cryoprotectant containing 20% maltodextrin and 2% dextrose (Neobiosys, France), lyophilized and the powder was stored at -20°C until use. The viability was checked regularly by plating appropriate serial dilution on the MRS agar plates and counting the colonies after incubation at 37°C for 48 hours. *Lactiplantibacillus plantarum*^{NIZO2877} (Lp^{NIZO2877}, formally *Lactobacillus*, reclassified based on (52), originally isolated from a sausage in Vietnam (kind gift from Prof. Michiel Kleerebezem, NIZO food research BV, Netherlands) were cultured overnight in MRS medium (Oxoid, Thermo Scientific, CM0359) at 37°C without agitation. Aliquots were centrifuged and after discarding the supernatant, the pellet was snap-frozen in liquid nitrogen and stored at -80°C . Lp^{NIZO2877} remained viable and no decrease in viability was observed during the experiment. For the mouse treatment, the lyophilized Lp^{WJL} was each day freshly dissolved in sterile PBS to the concentration 2×10^8 CFU/30 μl which corresponded to one treatment dose. Placebo for mouse treatment was created by dissolving lyophilized control cryoprotectant (non-inoculated control culture batch of the Lp^{WJL} lyophilized culture batch) in sterile PBS. Heat-killed bacteria were prepared as described for Lp^{WJL} and kept at 65°C for 30 min. Successful bacterial inactivation was verified by plating on the MRS agar plates and incubating at 37°C for 48 hours. Frozen pellet of Lp^{NIZO2877} cultures were dissolved in placebo to the concentration 2×10^8 CFU/30 μl . Lp^{WJL} and Lp^{NIZO2877} isolated cell wall was dissolved in placebo to

correspond to the 2×10^8 CFU/30 μl per treatment dose.

Purification of *L. plantarum* cell wall and preparation for mouse treatment

Purification of Lp^{WJL} and Lp^{NIZO2877} cell wall was performed as previously described (30). Briefly, *L. plantarum* cells were grown in MRS medium and harvested at mid-exponential phase. After washing with MilliQ water, the cells were boiled for 10 min and centrifuged at 5000g at 4°C . CFUs (3.75×10^{10}) were resuspended in 1 ml of SDS 5% in 50 mM of MES (Sigma-M8250) pH 5.5, pre-heated at 60°C and boiled for 25 min. After centrifugation at 20,000g, the pellets were resuspended in 1 ml of SDS 5% in 50 mM of MES pH 5.5, pre-heated at 60°C and boiled for 15 min and then washed with MilliQ water to remove SDS traces. Next, the pellets were sequentially enzymatically treated with 2 mg/ml of Pronase (Roche 165921) in 50 mM of MES (Sigma-M8250) at pH 6.0 for 90 min at 60°C ; 200 $\mu\text{g/ml}$ of trypsin (Sigma T-0303) in 50 mM of MES (Sigma-M8250) at pH 6.0 for 2 hours at 37°C with shaking; DNase (Sigma-D-4527) and RNase (Sigma-R-5503) (50 $\mu\text{g/ml}$) in 50 mM of MES (Sigma-M8250) at pH 6.0 for 1 hour at 37°C . After boiling for 15 min with SDS 2% in 50 mM of MES (Sigma-M8250) at pH 5.5 and centrifugation at 20,000g for 10 min, the pellets were washed with MilliQ water to remove SDS traces. Purified cell walls were lyophilized and stored at -80°C until use. Lp^{WJL} and Lp^{NIZO2877} isolated cell wall was dissolved in placebo to correspond to the 2×10^8 CFU/30 μl per treatment dose.

Extraction and analysis of peptidoglycan

L. plantarum strains were grown in MRS medium up to an OD_{600 nm} of 1. Cells were boiled in SDS, then treated with proteases, DNase and RNase as described above to prepare cell walls. The lyophilized material was then sheared with glass beads. The cell walls were resuspended in Milli-Q H₂O and the suspension was added to lysing matrix tubes containing 0.1 mm silica beads (MP Biomedicals). Tubes were homogenized with a MP Biomedicals FastPrep 24 Homogeniser (4.5 m/s intensity for 30 s). After centrifugation of the suspension at 200g for 1 min to remove glass beads, insoluble material containing cell walls was recovered by centrifugation 20,000g for 15 min. The pellet was resuspended in 4% SDS in 10 mM MES pH 5.5 for 15 min and boiled for 15 min. The final pellet was washed four times with 10 mM MES pH 5.5 and twice with MilliQ H₂O to remove SDS traces. The purified cell walls were lyophilized and treated with hydrofluoric acid (48%) for 19h at 0°C to remove covalently bound secondary cell wall polymers. The remaining insoluble purified peptidoglycan was washed twice with 250 mM Tris-HCl pH 8.0 and four times with MilliQ H₂O and

lyophilized. Peptidoglycan was digested with mutanolysin (Sigma Aldrich) and the resulting soluble muropeptides were reduced by NaBH₄ as described previously (53). The reduced muropeptides were separated by reverse phase ultra-high-pressure liquid chromatography (RP-UHPLC) with a 1290 chromatography system (Agilent Technologies) and a Zorbax RRHD Eclipse Plus C18 column (100 by 2.1 mm; particle size, 1.8 µm; Agilent Technologies) at 50°C using ammonium phosphate buffer and methanol linear gradient. The eluted muropeptides were detected by UV absorbance at 202 nm. Muropeptides were identified by LC-MS using an UHPLC instrument (Vanquish Flex, Thermo Scientific) connected to a Q-Exactive Focus mass spectrometer (Thermo Fisher Scientific). Muropeptides were quantified by integration of the peak areas of the UV profiles.

Intraperitoneal glucose tolerance test

At Day 50 after birth, animals were fasted for 5 hours (starting at 8 a.m.) before being intraperitoneally injected with D-glucose in sterile PBS (2 g/kg body weight; Merck, G7021). Glucose levels were measured by tail-tip bleeding with glucometer FreeStyle Lite (Abbott, Canada) before injection and 15, 30, 45, 60, 90, and 120 min after glucose administration.

FITC-dextran uptake assay

The intestinal permeability *in vivo* was measured by determination of the amount of FITC-dextran in blood after oral administration as described previously (54). Mice were fasted for 4 hours and then received 360 mg/kg b. w. of FITC-dextran (molecular weight 4.0 kDa; Merck, 46944) by intragastric gavage. Blood samples were obtained after 4 hours and serum was collected. The concentration of FITC-dextran was determined by spectrophotofluorometry (Safire2, Tecan Group Ltd., Switzerland) with an excitation wavelength of 483 nm and an emission wavelength of 525 nm using serially diluted FITC-dextran as standard.

Histology and morphometric analysis

Five cm long sections of mouse jejunum were collected, flushed with cold PBS, fixed in 4% paraformaldehyde-PBS at 4°C and processed by the Swiss-rolling technique (55). Subsequently, samples were processed by the Leica TP1020 tissue processor (Leica) and embedded into paraffin. Paraffin-embedded tissues were cut into 5-µm sections, dewaxed in a xylene bath and rehydrated in solutions of decreasing alcohol content before staining with hematoxylin and eosin (H&E) using standard techniques. H&E-stained tissues were visualized under a light microscope Leica DM6000 (Leica) and pictures were taken using LAS X software (Leica). Villous length and crypt depth were measured using Fiji 2.0.0 software. Segments of the jejunum and ileum were embedded in

TissueTec (Takara, Tissue-Tek® O.C.T. Compound) or fixed in 4% paraformaldehyde-PBS, swiss-rolled and embedded in tissue freezing medium (Leica) and subsequently frozen in vapors of liquid nitrogen and stored at -80°C until used. Cryosections (10 µm thick for the segments, 100 µm thick for the swiss rolls) were obtained on CM3050S Cryostat (Leica). Sections from the segments of jejunum and ileum were incubated with rabbit anti-Ki67 (1:100, AbCam, ab15580) and corresponding secondary antibody (1:400, Alexa Fluor 488, Life Technologies). The sections were mounted with VECTASHIELD® Antifade Mounting Medium with DAPI H-1200 (Thermo Scientific). Images were acquired using a Carl Zeiss LSM 780 inverted confocal microscope at a 20x magnification. Sections from the swiss rolls were incubated with rat anti-Ki67 (1:100, eBiosciences™, SolA15) and/or rabbit anti-villin (1:500, AbCam, ab130751) and with corresponding secondary antibody (1:400, Alexa Fluor 488 or Alexa Fluor 555, Invitrogen). Samples were mounted in ROTI Mount FluorCare DAPI (Roth) and image acquisition was performed using a Leica SP8 upright confocal microscope. Post-acquisition image analysis was performed with Fiji 2.0.0 software (56). Adjacent imaged fields were stitched together using the stitching tool available with the Fiji 2.0.0 software (57).

Stimulation of human embryonic kidney 293 cells stably transfected with TLRs and NODs

Human embryonic kidney (HEK) 293 cells stably transfected with plasmid carrying human (h)TLR2/CD14 gene were kindly provided by Prof. M. Yazdanbakhsh (Leiden, Netherlands), hTLR4/MD2/CD14 were a gift of Prof. B. Bohle (Vienna, Austria) and hNOD2 and hNOD1 expressing cells were purchased from InvivoGen (USA). Cells were stimulated for 20 hours in 96-well plates with Pam3CSK4 (5 µg/ml, InvivoGen, tlr1-pms), ultrapure LPS from *E. coli* O111:B4 (5 µg/ml, InvivoGen, tlr1-3pelps), muramyl dipeptide (MDP, 5 µg/ml, InvivoGen, tlr1-mdp) and L-Ala-γ-D-Glu-mDAP (Tri-DAP, 10 µg/ml, InvivoGen, tlr1-tdap) as positive or negative controls, respectively. Heat-killed *Lp*^{WJL} and *Lp*^{NIZO2877} and purified *Lp*^{WJL} and *Lp*^{NIZO2877} cell-wall dissolved in sterile PBS were used at concentrations corresponding to 10⁸ CFU/ml. *Lp*^{WJL} and *Lp*^{NIZO2877} purified PG and PG digested with mutanolysin (PGD) were tested at concentrations 100 µg/ml and 10 µg/ml, respectively. Concentrations of IL-8 were analyzed in cell supernatants by ELISA (Thermo Scientific) according to the manufacturer's instructions.

Serum factors measurement

At the end of experiment, blood was collected and left to clot at RT for 2 hours. Sera were

separated by centrifugation (2000g for 5 min, 4°C) and stored at -80°C until used. Levels of Insulin-like Growth Factor 1 (IGF-1) were measured by Mouse/Rat IGF-1 Quantikine ELISA (R&D systems) and insulin was measured by Ultrasensitive Mouse Insulin ELISA (Alpco, Salem, USA) according to manufacturer's instructions. G-CSF, IL-6, TNF-α, IL-1β and MCP-1 levels were determined by the custom multiplex Millipore Mouse Milliplex MAP Kit (Millipore Corp.) using the Bio-Plex System (Bio-Rad Laboratories, USA).

Liver IGF-1 measurement

Liver tissues were weighed and homogenized in lysis buffer containing PBS, 1% Triton X100 and a protease inhibitor mixture (Roche, cOmplete, EDTA-free Protease Inhibitor Cocktail). After centrifugation (12,000g for 10 min, 4°C) supernatants were collected and used at dilution 1:10 to determine the IGF-1 levels by Mouse/Rat IGF-1 Quantikine ELISA (R&D systems) according to manufacturer's instructions. Results are expressed as pg/mg of tissue.

Bone length measurement

Femur and tibia bones were removed at sacrifice, fixed in 4% of paraformaldehyde-PBS overnight at 4°C, washed with PBS and stored in 70% ethanol. Bone length was measured by digital caliper (Festa) and photographs of the bones were taken with Leica stereomicroscope M205FA.

RNA extraction and quantitative RT-PCR

Total RNA from liver, muscle and jejunum was isolated and purified using NucleoSpin RNA kit (Macherey-Nagel, iBioTech, 740984.250). Total RNA was quantified and assessed for purity using a NanoDrop ND-1000 Spectrophotometer (Thermo Scientific). Reverse transcription of 1 µg of RNA was performed using Superscript II enzyme (Invitrogen, 18064014) and random primers (Invitrogen, 48190011). Quantitative PCR was performed on a Biorad CFX96 apparatus (Biorad) using SYBRGreenER qPCR Supermix (Invitrogen, 11762500) for liver and muscle samples and Takyon™ No ROX SYBR Mastermix blue dTTP (Eurogentec, UFSMT-B0701) for jejunum samples, cDNA (1/100 dilution of the reverse transcription products) and gene specific primer sets (Supplementary Table 3). Melting curves of the detected amplicons were analyzed to ensure specific and unique amplification. PCR efficiency for each primer set was calculated using serial dilution of cDNA. For liver and muscle samples, *Tbp* (A) was used as an internal control to normalize gene expression using the 2^{-ΔCt} method (58). For jejunum samples, *Tbp* (B) and *Rpl32* were used as control genes to normalize target genes expression using the CFX Manager™ software (Biorad).

RNA sequencing

Total RNA from 1 cm piece of proximal jejunum was isolated and purified using NucleoSpin RNA kit (Macherey-Nagel, iBioTech, 740984.250). RNAs were quantified and assessed for purity using a NanoDrop ND-1000 Spectrophotometer (Thermo Scientific). Individually barcoded stranded mRNA-seq libraries were prepared from high quality total RNA samples (~500 ng/sample) using the New England Biolabs NEBNext RNA Ultra II Kit implemented on the liquid handling robot Beckman Coulter hybrid i7. Obtained libraries that passed the QC step were pooled in equimolar amounts; 2 pM solution of this pool was loaded on the Illumina sequencer NextSeq 500 and sequenced unidirectionally, generating ~500 million reads, each 85 bases long. Read quality was assessed by FastQC (59). STAR aligner (60) (version STAR_2.6.0a) was used to align the reads back to the GRCm38 reference genome. The gene count tables were generated during the alignment step using the GRCm38.99 annotation in gtf format. Raw read counts were used as an input for differential expression analysis. This analysis was carried out using DESeq2 Bioconductor package (v 1.34.0) in R (v 4.1.1), using mouse genotype as the main effect. During the data exploration with Principle Component Analysis, one of the Lp^{WJL} MAL replicates showed a discordant gene expression pattern compare to its sample group. The sample was therefore removed for the downstream analysis. Log2-fold change values calculated by DESeq2 were used for gene set enrichment analysis (GSEA) using clusterProfiler R Bioconductor package (v 3.14.3) using Gene ontology resource as gene set input.

Western blot analysis

Frozen liver samples were homogenized in RIPA Plus lysis buffer (50 mmol/L Tris-HCl pH7.4, 1% NP-40, 0.5% Na deoxycholate, 0.1% SDS, 150 mmol/L NaCl, 2 mmol/L EDTA and 50 mmol/L NaF) supplemented with 1× of protease inhibitors (Complete Protease Inhibitor Cocktail, Roche). After centrifugation of the lysates, protein concentration was estimated in the supernatant using a Pierce™ BCA Protein Assay Kit (Thermo Scientific, 23227). Total proteins (30 µg) were separated on 10% SDS-polyacrylamide gel (Euromedex, TO-A053-500G) or Mini-PROTEAN® TGX Precast Gels (Bio-Rad, #4561096) and then transferred to Immobilon-P Polyvinylidene fluoride membranes 0.22 µm (Merck Millipore, IPVH00010). Membranes were blocked with 5% BSA in TBS 1× Tween 0.1% for one hour before being probed overnight at 4°C with the following specific primary antibodies: rabbit monoclonal anti-total Akt (C67E7) (#4691) and rabbit monoclonal anti-phospho S473 Akt (D9E) (#4060) from Cell Signaling. After washing, Ab binding was revealed by incubation with horse-

radish peroxidase (HRP)-conjugated secondary antibodies (one-hour incubation at room temperature, anti-Rabbit IgG HRP-linked antibody, 1:10000, #172-1019, Bio-RAD) and ECL (Luminata Forte Western HRP Substrate, Millipore, WBLUF0100). Signals were recorded by the ChemiDoc XRS+ (Bio-Rad) or C-DiGit® Blot Scanner (Li-Cor) and quantified using Fiji 2.0.0 software (56).

Data treatment and statistics

Statistical analysis was performed with GraphPad Prism software version 8.4.2 for Windows (GraphPad Software, San Diego, California USA, www.graphpad.com) using one-way ANOVA with Tukey's post-test for multiple group comparison and two-tailed *t* test for comparison between two groups. Analysis of intestinal morphology and Ki67⁺ cell numbers was performed by the nested *t* test. Data in Fig. 6 were tested by two-way ANOVA to compare between genotypes and treatments. Values of *P* < 0.05 were considered statistically different. Data are expressed as the mean ± standard error of the mean (SEM) or dot plots with mean ± SEM.

REFERENCES AND NOTES

1. A. A. Butler, D. LeRoith, *Endocrinology* **142**, 1685–1688 (2001).
2. V. L. Tokarz, P. E. MacDonald, A. Klip, *J. Cell Biol.* **217**, 2273–2289 (2018).
3. C. J. Kenyon, *Nature* **464**, 504–512 (2010).
4. P. K. Fazeli, A. Klibanski, *J. Endocrinol.* **220**, R57–R65 (2014).
5. J. P. Thissen, J. M. Ketelslegers, L. E. Underwood, *Endocr. Rev.* **15**, 80–101 (1994).
6. L. V. Blanton, M. J. Barratt, M. R. Charbonneau, T. Ahmed, J. I. Gordon, *Science* **352**, 1533 (2016).
7. F. Leulier et al., *Cell Metab.* **25**, 522–534 (2017).
8. J. L. Gehrig et al., *Science* **365**, eaau4732 (2019).
9. M. I. Smith et al., *Science* **339**, 548–554 (2013).
10. M. Schwarzer et al., *Science* **351**, 854–857 (2016).
11. J. Yan et al., *Proc. Natl. Acad. Sci. U.S.A.* **113**, E7554–E7563 (2016).
12. A. Molinaro et al., *Mol. Metab.* **6**, 1371–1380 (2017).
13. G. Storelli et al., *Cell Metab.* **14**, 403–414 (2011).
14. E. M. Brown et al., *Nat. Commun.* **6**, 7806 (2015).
15. M. Kosek et al., *Clin. Infect. Dis.* **59**, S239–S247 (2014).
16. V. Owino et al., *Pediatrics* **138**, e20160641 (2016).
17. P. M. Ueno et al., *Am. J. Physiol. Gastrointest. Liver Physiol.* **301**, G612–G622 (2011).
18. J. L. Liu, D. LeRoith, *Endocrinology* **140**, 5178–5184 (1999).
19. E. Stratikopoulos, M. Szabolcs, I. Dragatsis, A. Klinakis, A. Efstratiadis, *Proc. Natl. Acad. Sci. U.S.A.* **105**, 19378–19383 (2008).
20. C. P. Hawkes, A. Grimberg, *Pediatr. Endocrinol. Rev.* **13**, 499–511 (2015).
21. S. Yakar et al., *Proc. Natl. Acad. Sci. U.S.A.* **96**, 7324–7329 (1999).
22. H. Werner, D. Weinstein, I. Bentov, *Arch. Physiol. Biochem.* **114**, 17–22 (2008).
23. R. K. Menon, M. A. Sperling, *Endocrinol. Metab. Clin. North Am.* **25**, 633–647 (1996).
24. B. K. Das, J. Ramesh, J. K. Agarwal, O. P. Mishra, R. P. Bhatt, *J. Trop. Pediatr.* **44**, 139–141 (1998).
25. W. Okitolonda, S. M. Brichard, J. C. Henquin, *Diabetologia* **30**, 946–951 (1987).
26. M. P. Chapot-Chartier, S. Kulakauskas, *Microb. Cell Fact.* **13** (Suppl 1), S9 (2014).
27. R. Sengupta et al., *Mediators Inflamm.* **2013**, 237921 (2013).
28. M. T. Sorbara, D. J. Philpott, *Immunol. Rev.* **243**, 40–60 (2011).

29. B. Erkosar et al., *Cell Host Microbe* **18**, 445–455 (2015).
30. R. C. Matos et al., *Nat. Microbiol.* **2**, 1635–1647 (2017).
31. H. Kozakova et al., *Cell. Mol. Immunol.* **13**, 251–262 (2016).
32. D. M. Underhill, *Immunol. Rev.* **219**, 75–87 (2007).
33. T. Kawai, S. Akira, *Cell Death Differ.* **13**, 816–825 (2006).
34. J. F. Cavallari et al., *Cell Metab.* **25**, 1063–1074.e3 (2017).
35. Y. G. Cao et al., *Cell Host Microbe* **30**, 1295–1310.e8 (2022).
36. A. Levy et al., *Proc. Natl. Acad. Sci. U.S.A.* **117**, 1994–2003 (2020).
37. R. M. Jones et al., *EMBO J.* **32**, 3017–3028 (2013).
38. M. J. Barratt et al., *Sci. Transl. Med.* **14**, eabk1107 (2022).
39. A. K. Pandey et al., *PLOS Pathog.* **5**, e1000500 (2009).
40. K. P. Kotredes, B. Thomas, A. M. Gamero, *Front. Immunol.* **8**, 410 (2017).
41. J. F. Cavallari et al., *Am. J. Physiol. Endocrinol. Metab.* **319**, E305–E314 (2020).
42. F. El Marjou et al., *Genesis* **39**, 186–193 (2004).
43. Z. Al Nabhani, G. Dietrich, J. P. Hugot, F. Barreau, *PLOS Pathog.* **13**, e1006177 (2017).
44. R. Caruso, N. Warner, N. Inohara, G. Núñez, *Immunity* **41**, 898–908 (2014).
45. D. J. Philpott, M. T. Sorbara, S. J. Robertson, K. Croitoru, S. E. Girardin, *Nat. Rev. Immunol.* **14**, 9–23 (2014).
46. G. Nigro, R. Rossi, P. H. Commere, P. Jay, P. J. Sansonetti, *Cell Host Microbe* **15**, 792–798 (2014).
47. S. Umar, *Curr. Gastroenterol. Rep.* **12**, 340–348 (2010).
48. R. P. Ferraris, H. V. Carey, *Annu. Rev. Nutr.* **20**, 195–219 (2000).
49. V. Mannar, R. Micha, "Global Nutrition Report 2020: Action on equity to end malnutrition" (Development Initiatives Poverty Research, 2020); <https://resourcecentre.savethechildren.net/document/global-nutrition-report-2020-action-equity-end-malnutrition/>.
50. L. Madisen et al., *Nat. Neurosci.* **13**, 133–140 (2010).
51. C. Postic et al., *J. Biol. Chem.* **274**, 305–315 (1999).
52. J. Zheng et al., *Int. J. Syst. Evol. Microbiol.* **70**, 2782–2858 (2020).
53. E. Bernard et al., *J. Biol. Chem.* **286**, 23950–23958 (2011).
54. D. Srutkova et al., *PLOS ONE* **10**, e0134050 (2015).
55. C. Moelenbeek, E. J. Ruitenberg, *Lab. Anim.* **15**, 57–59 (1981).
56. J. Schindelin et al., *Nat. Methods* **9**, 676–682 (2012).
57. S. Preibisch, S. Saalfeld, P. Tomancak, *Bioinformatics* **25**, 1463–1465 (2009).
58. K. J. Livak, T. D. Schmittgen, *Methods* **25**, 402–408 (2001).
59. S. Andrews, "FastQC: A quality control tool for high throughput sequence data" (Babraham Bioinformatics, 2010); <https://www.bioinformatics.babraham.ac.uk/projects/fastqc/>.
60. A. Dobin et al., *Bioinformatics* **29**, 15–21 (2013).
61. B. Glauner, *Anal. Biochem.* **172**, 451–464 (1988).

ACKNOWLEDGMENTS

We thank the anonymous reviewers for their insightful comments and suggestions; the EMBL GeneCore facilities for expert technical assistance with mRNA sequencing; and J. Valterová, S. Meisnerová, J. Jarkovská, B. Draboňová, M. Salomon-Mallet, and S. Palussiére for excellent technical assistance. **Funding:** The work in F.L.'s laboratory was supported by the FINOVI Foundation, the Fondation pour la Recherche Médicale (Equipe FRM DEQ.Q grant 20180339196), and the Agence Nationale de la Recherche (grant ANR-18-CE15-0011). Work in M.Sc.'s laboratory was supported by a Neuron Impuls grant from Neuron Fund, grants 18-07015Y and 21-19640M from the Czech Science Foundation, and by the Ministry of Education, Youth and Sports of the Czech Republic (EMBO installation grant 4139). M.Sc. was supported by a J. E. Purkyne Fellowship from the Czech Academy of Sciences. The work in the laboratories of H.V., I.B., and M.C. is supported by the INSERM National Program "Microbiota." F.D.V. was supported by a grant from Fondation des Treilles. The work in I.G.B.'s laboratory was supported by the Agence Nationale de la Recherche (grant ANR-16-CE15-0021). D.F. was supported by the Czech Science Foundation (grant 20-30350S). **Data and materials**

availability: All data are provided in the main manuscript. Sequencing data are available at the European Nucleotide Archive (<https://www.ebi.ac.uk/ena>) as project PRJEB56002. **Author contributions:** F.L. and M.Sc. conceived the project and designed the experiments with inputs from H.V., N.P., H.K., M.Š., I.G.B., and M.C. M.Sc., A.J., P.P., F.D.V., K.M., A.L., S.G., R.C.M., C.G., and A.-L.B. performed the mouse experiments at IGFL. M.Sc., U.K.G., D.S., T.N., P.P.H., and T.H. performed the mouse experiments in Laboratory of Gnotobiology. T.B., J.J.M.L., A.J., and D.F. analyzed the RNAseq data. T.B. and M.Sc. performed the Cre x TdTomato mouse experiments. P.C. and M.-P.C.-C. isolated and analyzed the bacterial peptidoglycan. M.Sc., F.L., U.K.G., P.P., F.D.V.,

K.M., A.J., A.L., D.S., S.G., P.P.H., R.C.M., C.G., A.-L.B., and T.H. analyzed the data. M.Sc. and F.L. wrote the manuscript with assistance by the remaining authors. **Competing interests:** F.L. and M.Sc. disclose that they are inventors of licensed patents (WO2015173386A1, WO2017137547A1, and WO2019034826A1) covering the use of specific probiotic strains for improving the juvenile growth of animals and humans. The remaining authors declare no competing interests. **License information:** Copyright © 2023 the authors, some rights reserved; exclusive licensee American Association for the Advancement of Science. No claim to original US government works. <https://www.science.org/about/science-licenses-journal-article-reuse>

SUPPLEMENTARY MATERIALS

science.org/doi/10.1126/science.ade9767

Figs. S1 to S13

Tables S1 to S3

Reference (61)

MDAR Reproducibility Checklist

[View/request a protocol for this paper from Bio-protocol.](#)

Submitted 20 September 2022; accepted 4 January 2023
10.1126/science.ade9767